Fluorapatite needle mats on vesicle walls of Apollo low-Ti basalt 15556 indicate a final-stage water-rich liquid

Yang Liu[1,*], Chi Ma[2,*]

[1]Jet Propulsion Laboratory, California Institute of Technology, Pasadena, CA 91109, USA. Email: yang.liu@jpl.nasa.gov

[2]Division of Geological and Planetary Sciences, California Institute of Technology, Pasadena, CA 91125, USA.

*Corresponding authors: Yang Liu (yang.liu@jpl.nasa.gov), Chi Ma (chima@caltech.edu)

Key Points

- Discovery of fluorapatite needles on vesicle walls of Apollo basalt reveals liquid flow from interior to vesicle walls
- Non-equilibrium growth of fluorapatite occurred from a final-stage water-rich liquid
- Changesite-(Y) is identified and characterized for the first time in Apollo samples

Abstract

Lunar vesicular basalt 15556 contains evidence of volatiles in the form of gas bubbles. We report two occurrences of apatite needle mats, forming flow patterns from the rock interior onto vesicle walls. The mats on vesicle walls are free of silicate minerals or glass. The apatite needles display aspect ratios (length to width) of 8 to 21, implying the presence of water vapor as shown by available experimental results. Although all apatites are fluorapatite, those on the wall contain lower F (higher inferred OH) and higher rare earth elements than nearly pure fluorapatite away from vesicles, indicating apatite needles in these mats formed from highly evolved water-rich melt. Collectively, the morphology, texture, and chemistry of the fluorapatite needles on vesicle walls support that these crystals grew rapidly and out-of-equilibrium from a final-stage liquid that changed water-bearing silicate-rich to silicate-poor water-rich during its flow from interior to the vesicle wall.

Keywords: acicular fluorapatite, changesite, Apollo basalt, the Moon, water

Plain Language Summary

We discovered fluorapatite needle mats on the surface of vesicles inside lunar basalt 15556. These needle mats look like they flow from inside the rock onto the walls of vesicles, coating surfaces along the way. Underneath the vesicle wall, the needles are embedded in glass or other minerals. On the vesicle wall, the needles are free of any silicates. In contrast, in non-vesicular parts of the rock, fluorapatite occurs as discrete grains. The composition of the fluorapatite within these mats contains higher OH than those formed in non-vesicular parts in the sample, which means they formed in a melt that was more OH-rich than those in non-vesicular parts inside the rock. The elongated shape, the texture of the mats, and the chemistry suggest that fluorapatite needles grow rapidly from an evolving melt. Initially the melt was a water-bearing silicate melt but it quickly transitioned into a final liquid that is silicate-poor and water-rich.

1. Introduction

Our understanding of magmatic water on the Moon has been evolving. Apollo samples bear evidence of volatile-powered volcanic activities in the form of vesicular basalts and pyroclastic volcanic beads. Because hydrous minerals were not unequivocally found in Apollo samples, it was generally regarded that the Moon is very dry. Volatiles involved were hypothesized to be CO (e.g., [*Sato*, 1979; *Fogel and Rutherford*, 1995], HF, HCl, or H_2S (e.g., [*Ustunisik et al.*, 2015]). In 2008, however, the view of water on the Moon shifted from the seminal discovery of residual H, F, Cl, and S in volcanic glass beads [*Saal et al.*, 2008]. In the subsequent years, additional evidence was provided through direct measurements of enriched H in apatite and plagioclase [*Jeremy W. Boyce et al.*, 2010; *McCubbin et al.*, 2010; *Greenwood et al.*, 2011; *Hui et al.*, 2013] and high amounts of H in olivine-hosted melt inclusions [*Hauri et al.*, 2011]. These studies suggest that the Moon was wet and the interior of the Moon contained a significant amount of H, likely in the form of OH, comparable to those in Earth's mantle.

Despite these findings, how homogeneous is OH inside the lunar mantle is debated [*Albarède et al.*, 2015]. Specifically, the enrichment of heavy isotopes of moderately volatile elements (Zn, Ga, Rb, K) and the depletion of these elements with respect to refractory elements (e.g., Fe,Ti?) were used to argue that the source of mare basalts have lost most if not all of these elements and enrichment of H was local anomalies [*Paniello et al.*, 2012; *Kato et al.*, 2015; *Wang and Jacobsen*, 2016; *Kato and Moynier*, 2017; *Pringle and Moynier*, 2017; *Tian et al.*, 2020]. Additionally, the preferred crystallization of fluorapatite over hydroxyapatite indicates OH-rich fluorapatite in mare basalts is only a feature of the late-stage melt inside the rock, not representative of the parent melts that mare basalts were derived from [*Boyce et al.*, 2014]. Some of these arguments could be explained by the outgassing of the parent magmas of mare basalts [*Chen et al.*, 2015; *Ni et al.*, 2017] and the ability to outgas K, Zn, Cu, and Na during lunar volcanic eruptions [*Ma and Liu*, 2019, 2023; *Liu and Ma*, 2022; *Su et al.*, 2023]. As such, how and when volatile and moderately volatile elements are lost from the Moon remain unconstrained owing to the limited understanding of outgassing mechanisms of these elements.

In the effort to study outgassing mechanisms through the study of vapor condensates, we also examined the vesicle (fossil gas bubble) walls in the vesicular basalt 15556. CT results showed that vesicles in 15556 are highly connected to interstitial pore space and cracks, rendering the loss of primary gas in these bubbles during the formation of this sample (Liu et al., 2023). However, our studies revealed surprising new discoveries. One finding is wide occurrence of multiple $Cu_{2-x}S$ coatings that drape over the surface of pyrrhotite grains on vesicle walls and $Cu_{2-x}S$ rosette at the edge of these coatings (Liu et al., 2023). The texture and chemistry of copper sulfide are consistent with precipitation from a late-stage aqueous liquid. Here we report the discovery of fluorapatite needle mats, forming patterns suggesting liquid flow from inside the rock to the surface of vesicle walls.

2. Methods

2.1. Samples

The highly vesicular low-Ti basalt Apollo 15556 (1542.3 grams, ~12 cm across) was collected about 60 meters northeast from the edge of Hadley Rille from an area in which rocks as large as 20 cm are common (Apollo 15 Sample catalog). The sample was barely in the soil, lacking fillets or much dust coating. The K-Ar age of Apollo 15556 is ~3.4 Ga [*Kirsten et al.*, 1972] but additional radiometric ages have not been measured.

We were allocated pristine chips (subsample 290) and polished thin sections (15556, 30 and 15556, 33). These thin sections were made from loose chips of the original parent samples 1 and 2, respectively. Thin section 30 and 33 were used to investigate the chemical, texture, and context of phosphate inside the rock.

Subsample 290 came from chip 223, a large fragment from the south side of the main rock (Fig. S1). The exact location of subsample 290 in 223 is unknown. Given the size of 223, subsample 290 would have been located a depth of <2 cm from the surface of the original rock. The subsample 290 contains six chips, each ranging from 5 mm to 1 cm in the largest dimension. We

examined four chips. The sample preparation procedure was similar to that in Ma and Liu (2019): the duration that the sample was exposed to the air was documented before the first measurement, then the time lapse was recorded for the subsequent measurements. The first chip (C1) was placed on a piece of carbon tape, coated with a thin layer of carbon (~20 nm thick) under 4×10^{-4} torr vacuum, and placed in a ZEISS 1550VP field emission scanning electron microscope (FE-SEM) under a 5×10^{-6} torr vacuum within 75 minutes of the opening of the N_2 bag. Two weeks after exposing the sample to air, two additional chips (C2 and C3) were mounted on carbon tapes, coated with carbon, and examined together with the first chip. Chip C3 was then turned upside down, coated with carbon, and examined again. The fourth chip (C4) was mounted on carbon tape and then directly examined without carbon coating together with C1 at 4 weeks after the bag was opened. We did not detect any changes of features observed in the sample.

2.2. Analytical Methods

We used the ZEISS FE-SEM to examine chips and polished thin sections. Accelerating voltages of 10 kV and 15 kV were used to obtain the secondary electron (SE) and backscatter electron (BSE) images of the sample. The compositions of minerals on vesicle walls were analyzed with an Oxford X-Max 80 mm^2 SDD Energy Dispersive Spectrometer (EDS) system attached to the SEM and obtained with an XPP correction procedure calibrated with Oxford factory internal standards (albite for Na, feldspar for K, FeS_2 for S, wollastonite for Ca, SiO_2 for Si, MgO for Mg, Al_2O_3 for Al, pure metals for Ti, Cr, Mn, Fe and Zn). We showed previously that the SEM-EDS data of several electron probe standards (anhydrite, anorthite, fayalite, basaltic glasses) are in excellent agreement with certified values for most elements except that FeO displays 15-18% relative differences at 10 kV [*Liu and Ma*, 2022]. Additionally, our previous study showed that SEM-EDS data of rough pyrrhotite on the vesicle wall are similar to SEM-EDS data of pyrrhotite in polished sections [*Liu et al.*, 2023].

Chemistry of apatite and other minerals in the thin sections (15556, 30 and 15556, 33) was quantified using a field emission electron probe microanalyzer (FE EPMA) JEOL JXA-iHP200F. The phosphates are challenging due to their small sizes and the need to measure rare earth elements (REEs). We used three setups. Setup 1 is optimized for the small grains using a defocused beam (~0.5 um diameter) of 10 nA current and excited at 10 kV. This setup includes P, Si, Fe, Mg, Ca, Na, Ce and Nd. Setup 2 is optimized for Y and selected rare earth elements using a defocused beam (0.5-2 μm diameter) of 20 nA current and excited at 20 kV. Setup 3 used a beam of 1 μm diameter excited at 15 kV and 20 nA, including additional REE elements and Al. Calibration used natural and synthetic standards, including Durango apatite (Ca *K*α, P *K*α), anorthite (Si *K*α, Al *K*α), fayalite (Fe *K*α), sodalite (Cl *K*α), albite (Na *K*α), phlogopite (F Kα), YPO_4 (Y *L*α), $LaPO_4$ (La *L*α), $CePO_4$ (Ce *L*α), $PrPO_4$ (Pr *L*α), $NdPO_4$ (Nd *L*α), $SmPO_4$ (Sm *L*α), $GdPO_4$ (Gd *L*α), $DyPO_4$ (Dy *L*α), $ErPO_4$ (Er *L*α), $YbPO_4$ (Yb *L*α). Changesite-(Y) and ferromerrillite are more beam sensitive than apatite. For silicates and Fe-Cr-Ti oxides, we used an electron beam with a diameter of 8 μm at 15 kV and 20 nA. Natural and synthetic standards are used, including microcline (K *K*α), albite (Na *K*α), forsterite (Mg *K*α), anorthite (Al *K*α, Si *K*α, Ca *K*α), TiO_2 (Ti *K*α), Cr_2O_3 (Cr *K*α), Mn_2SiO_4 (Mn *K*α), fayalite (Fe *K*α). About 14 plagioclase, 27 pyroxene, 10 olivine, 5 Fe-Cr-Ti-oxides, and 4 ilmenite grains in 15556, 30 were analyzed with EPMA. All analyses were processed using the CITZAF correction procedure. All elements were counted for 20 seconds at

peak positions, and Na was measured first to limit Na loss. The mean atomic number method [*Donovan and Tingle*, 1996] was used for the background correction of each element.

3. Results

3.1. Fluorapatite Needles on Vesicle Walls

We observed two occurrences of apatite needle mats on vesicle walls among four chips examined (locations in Fig. S2). These needle mats form linings extending from walls of holes in vesicle walls onto the vesicle wall. Long axes of these needles are aligned in directions, suggesting flow around the hole (Figs. 1, 2, and S3). This texture is better viewed in the stereo image shown in Fig. S4. The length of needles ranges from 2 to 26 μm and the width ranges from 0.3 to 3.2 μm. Most grains display large aspect ratios (length/width) of 8-21, whereas a few small ones are more equant of aspect ratios of 2-7. Two occurrences have some distinct differences. In the occurrence in Chip C1, nearly all needles are solid in the center and those inside the hole are mixed with ~1 μm-sized euhedral ilmenite and a Zr-rich mineral, possibly zirconolite, $(Ca,Y)Zr(Ti,Mg,Al)_2O_7$ (Fig. 1). In the occurrence in Chip C3, almost all apatite needles are hollow (Fig. 2). Those hollow tubes on the wall of the hole are embedded in Si-rich glass whereas those on the vesicle wall are free of any glass (Fig. 2). Despite of these differences, apatite needle mats on the vesicle walls in both occurrences are free of any silicate glass. SEM-EDS measurements of these needles suggest that they are fluorapatite with no detectable Cl, although the amount of OH cannot be determined.

The 3D arrangement of apatite needles on vesicle walls are not easily preserved during the preparation of polished sections, we would have missed these mats on vesicle walls if only polished sections were examined. Figure 3 shows the best possible 2D presentation of the occurrence in Figure 2 in a polished section. Center cavities are viewable for grains cut parallel to and perpendicular to *c* axis. Long axes of these grains form a flow pattern around the vesicles with some protruding into the vesicles or attached to the wall of vesicles. Since we do not have the knowledge of the rock above or below the polished section, it is unclear if the flow pattern extends to larger round vesicles. Another vestige of apatite needle clusters is few apatite grains on the walls of openings that connected to larger vesicles (Fig. S5).

3.2. Phosphates in Mesostasis of Apollo 15556

Apollo 15556 is a holocrystalline low-Ti basalt, consisting of interlocking euhedral pyroxene grains (<0.6 mm) and plagioclase laths (<2.5 mm and width of <0.1 mm) with minor amount of euhedral olivine grains (up to ~1 mm in the largest dimension). These phenocrysts show normal zoning due to crystallization under cooling (Fig. S6, Table S1). After extensive crystallization, diverse minerals grew intimately from the late-stage melt, forming mesostasis. Visual estimate suggests ~5 vol% of each thin section is made of mesostasis. Typical minerals in mesostasis include Fe-rich augite ($En_{\sim 2}Fs_{\sim 60}Wo_{\sim 38}$), fayalite ($Fo_{xx}$), plagioclase ($An_{\sim 80}$), ilmenite, troilite with Fe metal inclusions, glass with Ba-bearing potassium feldspar, silica, phosphates, and

occasional Zr-rich accessory minerals (tranquillityite, zirconolite, baddeleyite). Fayalite often displays sieve texture with many inclusions. Three types of phosphate appear in mesostasis, including changesite-Y [$(Ca_8Y)\square Fe(PO_4)_7$], ferromerrillite, and fluorapatite (Figs. 4 and S6). As discussed above, ferromerrillite or changesite-(Y) does not occur on vesicle walls (Figs. 1-3).

3.3. Chemistry of Phosphates

The small sizes of fluorapatite needles (cross-section <1 μm) on the wall make is difficult to obtain precise determination of Y and rare earth elements (REEs), which requires higher excitation voltage that would lead to more contamination from neighboring silicates. For wall apatite chemistry, we combined Setup 1 and 2 (Table S2). Setup 1 with the low voltage (10 kV) provides better spatial resolution so major and minor elemental contents, including Ce and Nd, are more accurate. Setup 2 with a high voltage (20 kV) provides better counting statistics for Y and REEs with <0.2 wt% concentration. However, Setup 2 also incurred more contamination as shown by higher SiO_2 and FeO contents and lower Ce and Nd contents than Setup 1 in the same grain. Therefore, we used Y and REEs (except for Ce and Nd) values from Setup 2 and the rest from Setup 1 for fluorapatite, noting that the Y and other REEs are lower than their real values. Compositions of additional fluorapatite in rock matrix were analyzed using Setup 3 (Table S2).

We chose large phosphate grains in mesostasis for the EPMA analyses. Results from three setups are similar. A new phosphate mineral, changesite-(Y), was discovered in samples returned by Chang'e-5 mission (Li et al. 2022), although it was previously classified as merrillite in Apollo rocks and lunar meteorites [*Jolliff et al.*, 2006]. Our analyses of changesite-(Y) in 15556 are similar to those in 15475 and LaPaz basaltic lunar meteorites. The EPMA oxide totals of ferromerrillite in the mesostasis are low (Table S2). The low totals cannot be explained by any unanalyzed elements with atomic number >10, as SEM-EDS did not reveal any elements of 0.1 wt% or higher. The third EPMA setup included all REEs but the unanalyzed REE in Setup 1 and 2 are below the detection of Setup 3, and these REEs add up to <0.5 wt%.

Fluorapatite needles (Figs. 3 and S5) on vesicle walls are more enriched in REE and depleted in F than those larger grains (Figs. 4 and S6) in mesostasis (Fig. 5, Table S2). There are some overlaps in composition between fluorapatite near vesicles and those in mesostasis. However, since we lack the information of the third dimension of the thin sections, some of the mesostasis may be also linked to vesicles (Figs. 3 and S6). Overall, the chemical variation of fluorapatite suggests a progressive enrichment of incompatible elements (REEs) and OH in the late-stage melt with crystallization. The wall fluorapatite with highest calculated OH (Table S2) reflects the final liquid is water rich.

4. Discussion

The 3D arrangement of fluorapatite needle mats in Apollo 15556 have never been reported previously. McKay et al. (1972) observed individual, free-standing Cl-rich apatite grains on vug walls in Apollo 14 breccias, which are euhedral, but more stubby and much larger (width of 12 μm and length up to ~50 μm) than those observed in 15556. McKay et al. (1972) proposed these

free-standing apatite grains were deposited by vapor. However, vapor deposit cannot explain the texture and petrological association of fluorapatite needle mats in Apollo 15556. The arrangement of fluorapatite needles indicates they were aligned by flowing fluids. These needles coat the vesicle walls and are not protruding to space as free-standing crystals. Beneath vesicle wall, fluorapatite needles are fully embedded in silicate glass or minerals, suggesting their initial formation in silicate melt. The μm-sized zirconolite and ilmenite grains interstitial to fluorapatite needles are unlikely to be deposited by vapor since Zr and Ti are refractory and non-volatile elements. Additionally, the higher contents of REEs and OH in wall fluorapatite than those in mesostasis indicate wall fluorapatite formed from a more evolved liquid than those in the rock matrix. Based on the above evidence, we propose the fluorapatite needle mats on vesicle walls in Apollo 15556 formed by rapid precipitation in the very last liquid after the rock is nearly fully solidified.

Experiments showed that apatite needles, often with a hollow center, precipitate from a liquid under non-equilibrium conditions [*Wyllie et al.*, 1978]. Needles formed when a vapor phase is absent are much elongated (length/width >20) that those when a water vapor phase is present (length/width >10) [*Wyllie et al.*, 1978]. Aspect ratios of apatite needles in Apollo 15556 are generally <20, indicating the final-liquid possibly coexisted with a vapor phase.

Vesicular basalt 15556 is located near the top of a lava flow and exposed to the vacuum in the space at the late stage of its sonification [*Liu et al.*, 2023]. When the final-liquid formed near the round vesicles, they were pulled to the vesicle while apatite quickly grows from a cooling melt. Along its flow toward the vesicle wall, most silicates would have formed leaving the final stage of liquid water rich as evidenced by nearly pure apatite needle mats on vesicle wall. Together with the observation of copper sulfide precipitates on the surface of troilite grains on vesicle walls [*Liu et al.*, 2023], the finding of apatite needles on vesicle walls supports the presence of aqueous liquid at the final stage of the solidification of 15556.

Apatite is now commonly used to infer the geochemical character of magmatic water in the parent basalt and in the mantle. However, partition of F, Cl, and OH between apatite and melt is such that high OH contents of apatite only occur after the extensive fractionation of the melt and do not have a high fidelity to the water contents of the parent melt [*Boyce et al.*, 2014]. The silicate-free needle mats, high REE contents and low F contents in fluorapatite needles near vesicle walls are consistent with a final liquid that is water-rich and silicate-poor. These needle mats are not easily preserved in a polished section but rapidly-grown apatite are identifiable given the large aspect ratio (acicular or needle shape) and the hollow center. Many apatite grains previously measured for the OH contents or isotopes display these rapid-growth features (e.g., 12039, 12040, 12064, 15016, 15065, 15058, 75055) [*Boyce et al.*, 2015; *Treiman et al.*,2016; *Barnes et al.*, 2019]. Hollow or skeletal apatite grains in 12040 and other Apollo 15 basalts are comparable to those in 15556 in size, but occur in fewer numbers or are fully embedded in silicates [*Boyce et al., 2015; Barnes et al., 2019*] (Fig. S8). Experimental data are lacking for the partition of F, OH and Cl and their isotope fractionations between apatite, melt, and vapor under non-equilibrium conditions. Thus, inferring the geochemical nature of parent melt is further complicated by these non-equilibrium cases. One needs to perform detailed textural analyses and

exercise caution when using apatite to constrain original magmatic contents in basaltic melts and in mantle source.

5. Conclusions

Direct observation of Apollo vesicular basalt 15556 revealed interesting processes at the very late stage of the solidification of the sample. Fluorapatite needles, often with hollow centers, form mats extending from the wall of openings on vesicle walls to the surface of vesicle walls. Long axes of needles are aligned in patterns suggestive of flow around the opening. Based on the lack of silicates between needles on vesicle walls and presence of them inside the opening, the flow is likely originated from the interior of the rock as a water-rich silicate melt but becomes water-rich liquid when it reached to the surface of the vesicle wall. Together with observations of copper sulfide coatings and rosettes on top of pyrrhotite on vesicle walls, our new findings suggest the last stage liquid of volatile-rich basalt is not well understood, but is important and critical for the overall volatile evolution on the Moon.

Acknowledgements

We are grateful to the Lunar Curation Office for allocating Apollo 15556 chips and polished sections, and for providing the processing history of the allocated subsample. The research was performed at the Jet Propulsion Laboratory, California Institute of Technology, under a contract with the National Aeronautics and Space Administration (80NM0018D0004), and SEM and EPMA analyses were carried out at the Caltech GPS Division Analytical Facility, which is supported, in part, by NSF Grants DMR-0080065 and EAR-2117942

Data Availability Statements

Upon acceptance of the paper, supplementary Table S1 and S2, reporting compositions of phosphates and silicates, will be deposited at the JPL's Open Repository with DOIs.

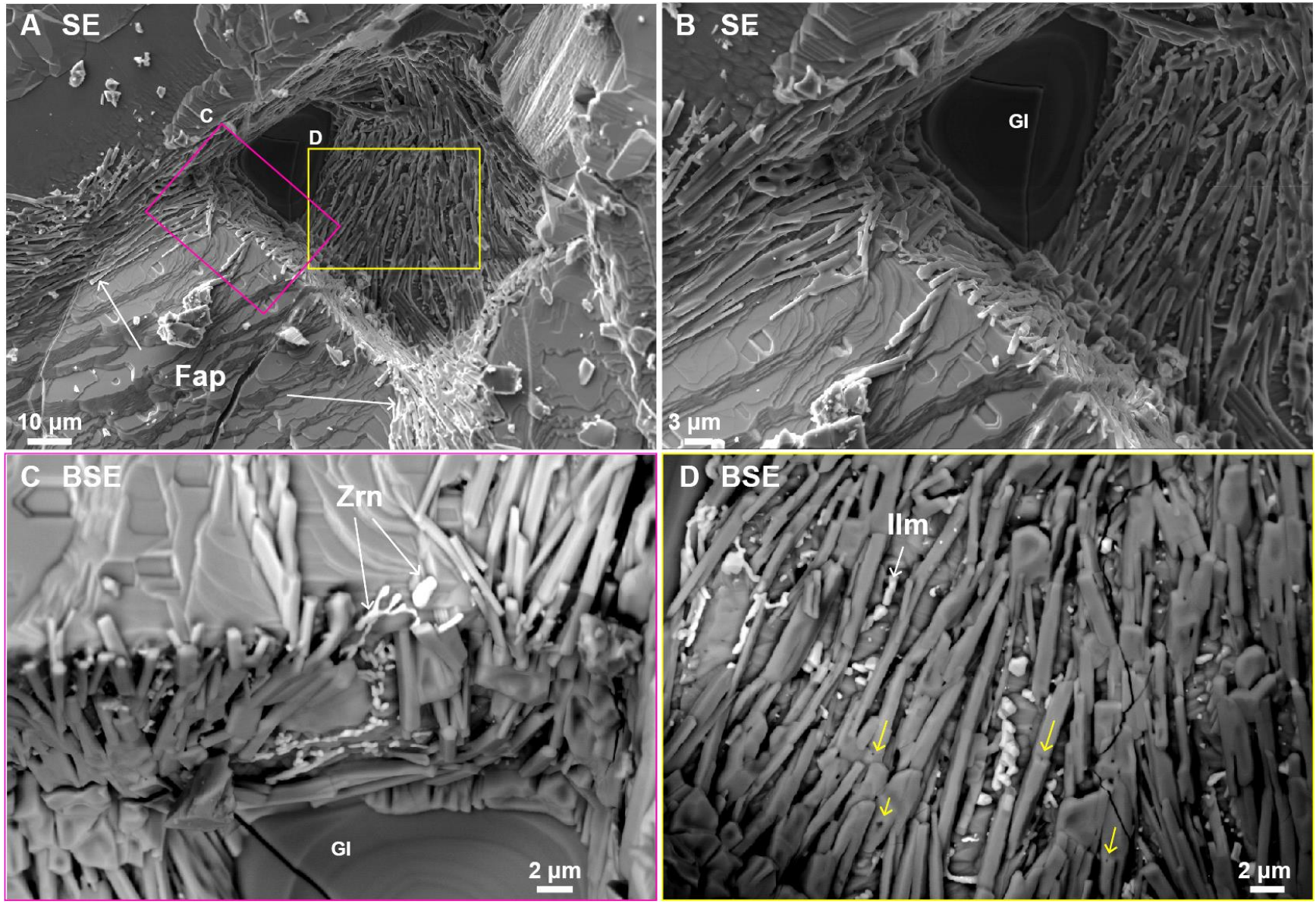

284

285 **Figure 1**. Fluorapatite (Fap) needles lining a square hole on a vesicle wall in Chip C1. (A) Secondary electron (SE) image of the
286 needles with long axes following a flow pattern. Magenta and yellow boxes show area in (C) and (D), respectively. (B) SE image at a
287 higher magnification than (A), showing some needles protruding into the space. (C) Backscatter electron (BSE) image showing apatite
288 needles intermingled with a Zr-mineral (possibly zirconolite, Zrn). (D) BSE image of the area in yellow box in (A), showing some
289 fluorapatite needles are hollow in the center (yellow arrows) with ilmenite (Ilm). Full sized images are shown in Figure S3.
290

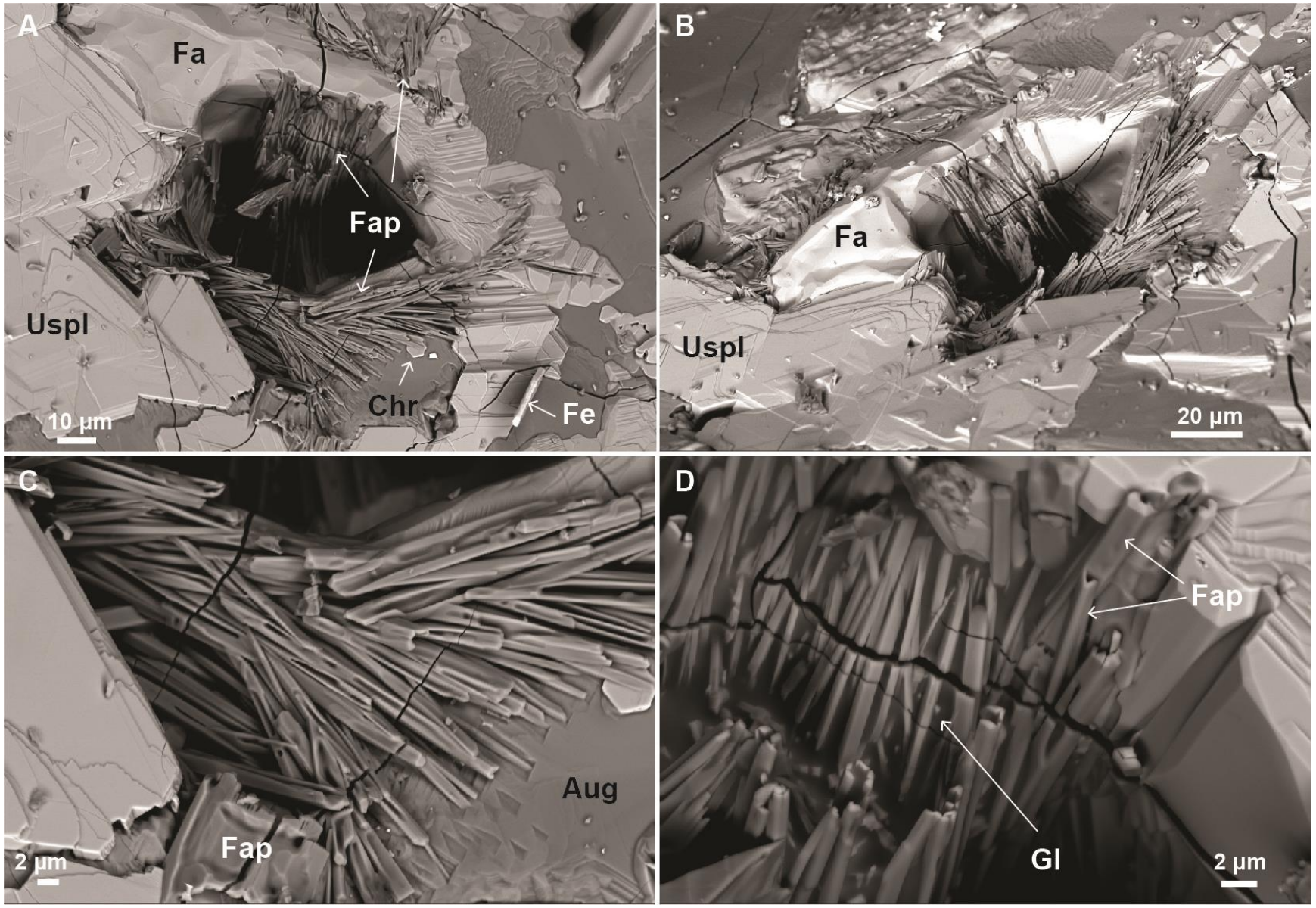

291

Figure 2. BSE images of fluorapatite (Fap) needles around and in a hole in a vesicle wall in Chip C3. (A) The needles following a flow pattern either into or out of the hole. (B) An oblique view of the hole. (C) Many needles are hollow. (D) Needles inside the hole are mixed with glass, many are clearly hollow in the center. Aug, augite; Chr, chromite; Fe, Fe metal; Fa, fayalite; Uspl, ulvöspinel; Gl, glass. Full sized images are shown in Figure S3.

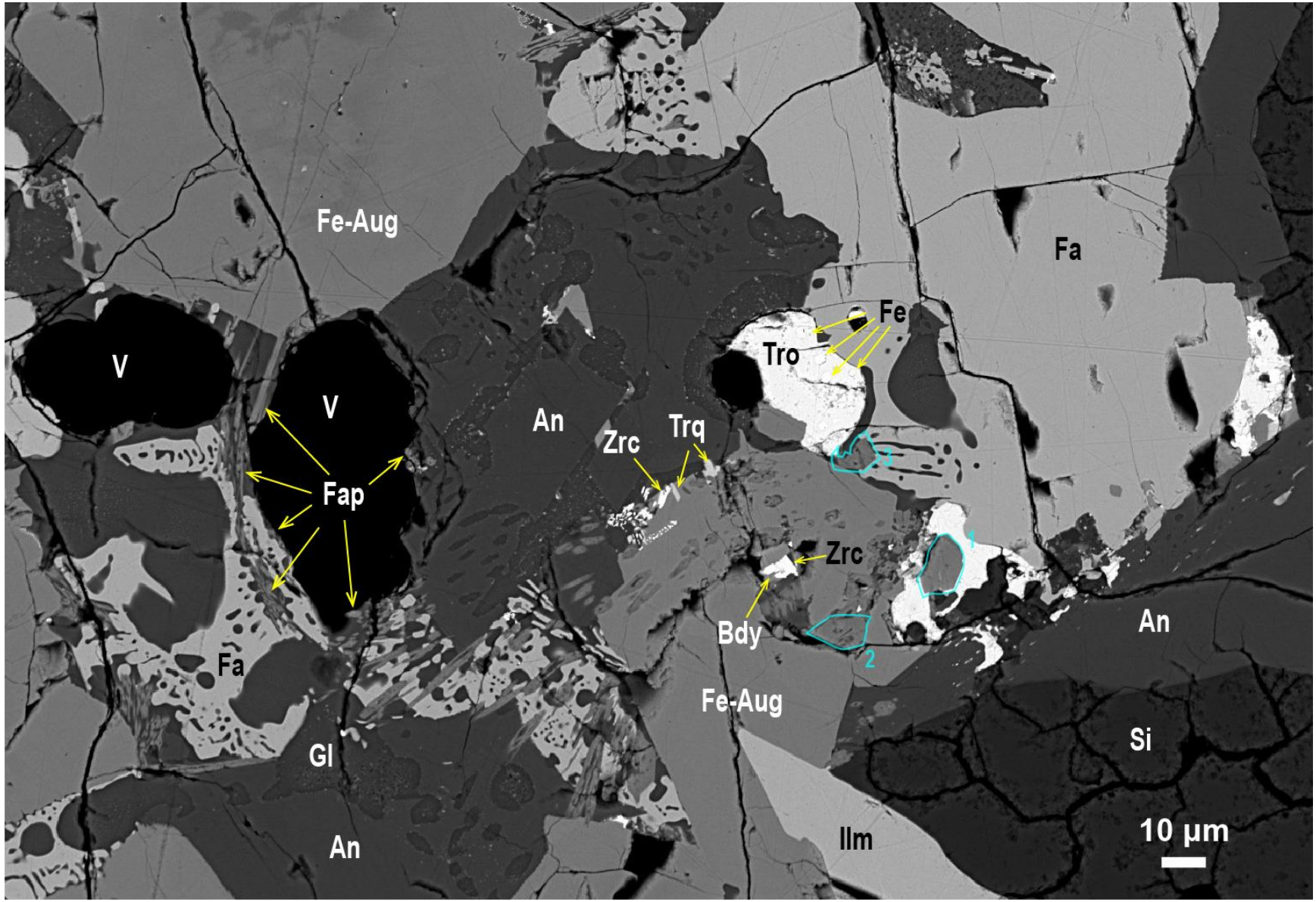

297

298 **Figure 3**. Arrangement of fluorapatite (Fap) in polished section 15556, 33 around vehicles (V), resembling the needle piles on vesicle
299 walls. Yellow arrows point to apatite needles protruding into the vesicle. There are numerous fluorapatite needles with empty centers
300 in this area intergrown with fayalite (Fa), Fe-augite (Fe-Aug, ~$En_2Fs_{59}Wo_{39}$), anorthite (An, ~An_{80}), and K-Ba-rich glass (Gl). Blocky
301 apatite grains analyzed with EPMA are outlined in cyan and numbers are the same as in Table S2. Other phases are: ilmenite (Ilm),
302 troilite (Tro), Fe-metal (Fe), zirconolite (Zrc), baddeleyite (Bdy), tranquillityite (Trq), and a silica phase (Si).

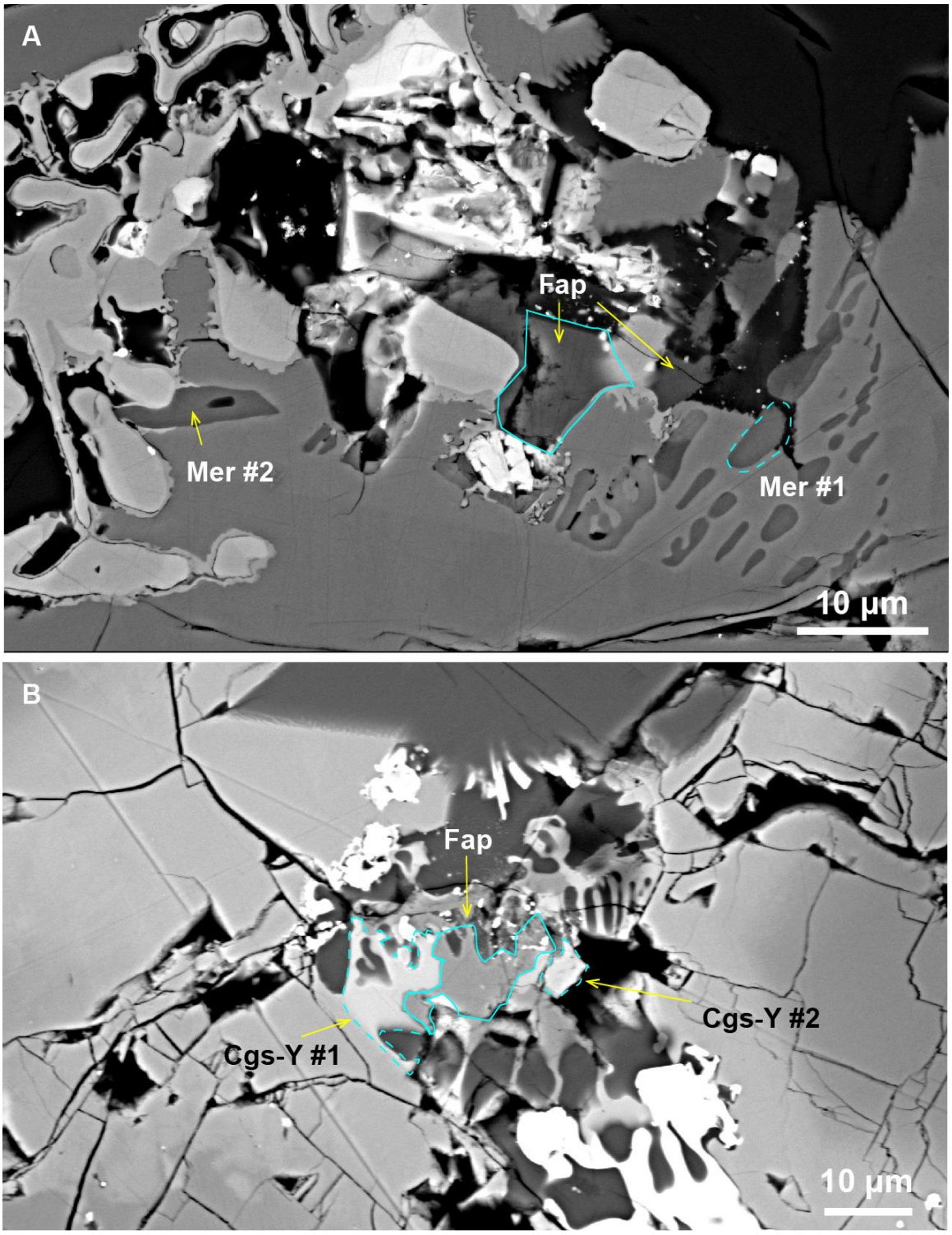

Figure 4. BSE images of fluorapatite (Fap), changesite-(Y) (Cgs-Y), and merrillite (Mer) in the mesostasis. (A) An area in polished section 15556, 30. (B) An area in polished section 15556, 33. Grains analyzed with EPMA are outlined by cyan lines for fluorapatite and cyan dashed lines for ferromerrillite and changesite-(Y), respectively. Numbers correspond to those in Table S2.

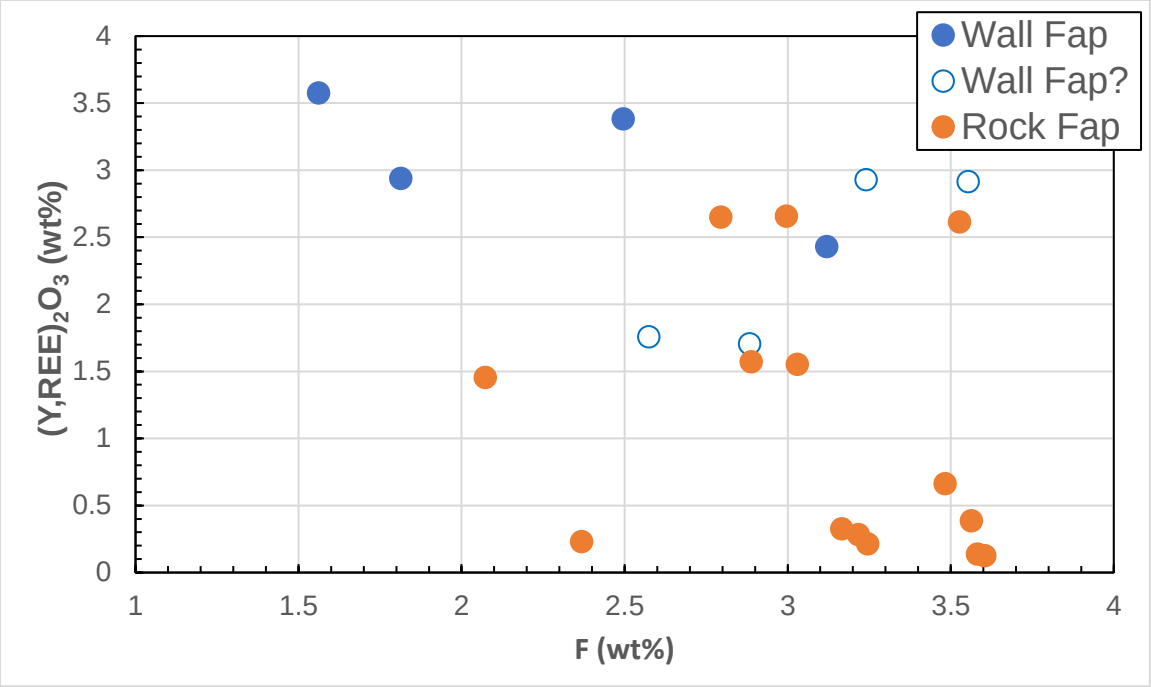

Fig. 5. Variation of F and (Y, REE)$_2$O$_3$ contents in fluorapatite (Fap) grains with their petrographic context. Wall Fap are those in Fig. S5, the open circles are larger grains in the same region from which the fluorapatite needle clusters also formed (Fig. 3), rock Fap refers to those in Figs. 4 and S6. Data used in this plot are normalized from raw data in Table S2.

References

Albarède, F., E. Albalat, and C.-T. A. Lee (2015), An intrinsic volatility scale relevant to the Earth and Moon and the status of water in the Moon, *Meteoritics & Planetary Science*, *50*(4), 568-577.

Barnes, J. J., I. A. Franchi, F. M. McCubbin, and M. Anand (2019), Multiple reservoirs of volatiles in the Moon revealed by the isotopic composition of chlorine in lunar basalts, *Geochim. Cosmochim. Acta*, *266*, 144-162.

Boyce, J. W., S. M. Tomlinson, F. M. McCubbin, J. P. Greenwood, and A. H. Treiman (2014), The Lunar Apatite Paradox, *Science*, *344*(6182), 400-402.

Boyce, J. W., Y. Liu, G. R. Rossman, Y. Guan, J. M. Eiler, E. M. Stolper, and L. A. Taylor (2010), Lunar apatite with terrestrial volatile abundances, *Nature*, *466*(7305), 466-469.

Boyce, J. W., A. H. Treiman, Y. Guan, C. Ma, J. M. Eiler, J. Gross, J. P. Greenwood, and E. M. Stolper (2015), The chlorine isotope fingerprint of the lunar magma ocean, *Science Advances*, *1*(8), e1500380.

Chen, Y., Y. Zhang, Y. Liu, Y. Guan, J. Eiler, and E. M. Stolper (2015), Water, fluorine, and sulfur concentrations in the lunar mantle, *Earth Planet. Sci. Lett.*, *427*, 37-46.

Donovan, J. J., and T. N. Tingle (1996), An Improved Mean Atomic Number Background Correction for Quantitative Microanalysis, *Microscopy and Microanalysis*, *2*(1), 1-7.

Fogel, R. A., and M. J. Rutherford (1995), Magmatic volatiles in primitive lunar glasses: I. FTIR and EPMA analyses of Apollo 15 green and yellow glasses and revision of the volatile-assisted fire-fountain theory, *Geochim. Cosmochim. Acta*, *59*(1), 201-215.

Greenwood, J. P., S. Itoh, N. Sakamoto, P. Warren, L. Taylor, and H. Yurimoto (2011), Hydrogen isotope ratios in lunar rocks indicate delivery of cometary water to the Moon, *Nature Geosci*, *4*(2), 79-82.

Hauri, E. H., T. Weinreich, A. E. Saal, M. C. Rutherford, and J. A. Van Orman (2011), High Pre-Eruptive Water Contents Preserved in Lunar Melt Inclusions, *Science*, *333*(6039), 213-215.

Hui, H., A. H. Peslier, Y. Zhang, and C. R. Neal (2013), Water in lunar anorthosites and evidence for a wet early Moon, *Nature Geosci*, *6*(3), 177-180.

Jolliff, B. L., J. M. Hughes, J. J. Freeman, and R. A. Zeigler (2006), Crystal chemistry of lunar merrillite and comparison to other meteoritic and planetary suites of whitlockite and merrillite, *American Mineralogist*, *91*(10), 1583-1595.

Kato, C., and F. Moynier (2017), Gallium isotopic evidence for extensive volatile loss from the Moon during its formation, *Science Advances*, *3*(7).

Kato, C., F. Moynier, M. C. Valdes, J. K. Dhaliwal, and J. M. D. Day (2015), Extensive volatile loss during formation and differentiation of the Moon, *Nature Communications*, *6*, 7617.

Kirsten, T., J. Deubner, P. Horn, I. Kaneoka, J. Kiko, O. A. Schaeffer, and S. K. Thio (1972), The rare gas record of Apollo 14 and 15 samples, *Lunar and Planetary Science Conference Proceedings*, *3*, 1865-1889.

Li, T., Li, Z., Huang, Z., Zhong, J., Fan, G., Guo, D., Qin, M., Zhang, J., Li, J., Liu, H., Qiu, L., Wang, F., He, S., Yu, A., Liu, R., Wu, Y., Deng, L., Tai, Z., He, Y. and Lin, Y. (2022) Changesite-(Y), IMA 2022-023. CNMNC Newsletter 69. *Mineralogical Magazine*, 86, 988.

Liu, Y., and C. Ma (2022), Direct evidence of volcanic outgassing of Na and K on the Moon from Apollo orange beads, *Icarus*, *382*, 115044.

Liu, Y., C. Ma, and S. A. Eckley (2023) Copper sulfide in a vesicular basalt implies aqueous liquid on the Moon.

Ma, C., and Y. Liu (2019), Discovery of a zinc-rich mineral on the surface of lunar orange pyroclastic beads, *American Mineralogist*, *104*(3), 447-452.

Ma, C., and Y. Liu (2023) Nanomineralogy of lunar beads: Discovery of zinc sulfide (ZnS) nanocrystals on a yellow bead fragment, condensed from volcanic vapors on the Moon. 54th Lunar and Planetary Science Conference, Abstract #1420.

McCubbin, F. M., A. Steele, E. H. Hauri, H. Nekvasil, S. Yamashita, and R. J. Hemley (2010), Nominally hydrous magmatism on the Moon, *Proceedings of the National Academy of Sciences*, *107*(25), 11223-11228.

McKay, D. S., U. S. Clanton, and D. A. Morrion (1972) Vapor phase crystallization in Apollo 14 breccia. *Proceedings of the Third Lunar Conference, Suppl. 3, Geochemica et Cosmochimica Acta*, 1, 739-752.

Ni, P., Y. Zhang, and Y. Guan (2017), Volatile loss during homogenization of lunar melt inclusions, *Earth Planet. Sci. Lett.*, *478*, 214-224.

Paniello, R. C., J. M. D. Day, and F. Moynier (2012), Zinc isotopic evidence for the origin of the Moon, *Nature*, *490*, 376.

Pringle, E. A., and F. Moynier (2017), Rubidium isotopic composition of the Earth, meteorites, and the Moon: Evidence for the origin of volatile loss during planetary accretion, *Earth Planet. Sci. Lett.*, *473*, 62-70.

Saal, A. E., E. H. Hauri, M. Lo Cascio, J. A. Van Orman, M. C. Rutherford, and R. F. Cooper (2008), Volatile content of lunar volcanic glasses and the presence of water in the Moon's interior, *Nature*, *454*(7201), 192-196.

Sato, M. (1979), The driving mechanism of lunar pyroclastic eruptions inferred from the oxygen fugacity behavior of Apollo 17 orange glass, *Proceedings of the Lunar and Planetary Science Conference, 10th*, 311-325.

Su, X., Y. Zhang, Y. Liu, and R. M. Holder (2023), Outgassing and in-gassing of Na, K and Cu in lunar 74220 orange glass beads, *Earth Planet. Sci. Lett.*, *602*, 117924.

Tian, Z., B. L. Jolliff, R. L. Korotev, B. Fegley, K. Lodders, J. M. D. Day, H. Chen, and K. Wang (2020), Potassium isotopic composition of the Moon, *Geochim. Cosmochim. Acta*, *280*, 263-280.

Treiman, A. H., J. W. Boyce, J. P. Greenwood, J. M. Eiler, J. Gross, Y. Guan, C. Ma, and E. M. Stolper (2016), D-poor hydrogen in lunar mare basalts assimilated from lunar regolith, *American Mineralogist*, *101*(7), 1596-1603.

Ustunisik, G., H. Nekvasil, D. H. Lindsley, and F. M. McCubbin (2015), Degassing pathways of Cl-, F-, H-, and S-bearing magmas near the lunar surface: Implications for the composition and Cl isotopic values of lunar apatite†, *American Mineralogist*, *100*(8-9), 1717-1727.

Wang, K., and S. B. Jacobsen (2016), Potassium isotopic evidence for a high-energy giant impact origin of the Moon, *Nature*, *538*, 487.